Journal of Nanobiotechnology

RESEARCH

Open Access

Cationic conjugated polymer coupled non-conjugated segments for dually enhanced NIR-II fluorescence and lower-temperature photothermal-gas therapy

Kexi Liu[1], Danni Hu[2,3], Liuliang He[2], Zhichao Wang[2], Peng Cheng[3], Pengfei Sun[3*], Yingying Chen[4*] and Daifeng Li[2*]

Abstract

The lack of a simple design strategy to obtain ideal conjugated polymers (CPs) with high absorbance and fluorescence (FL) in the near-infrared-II (NIR-II; 1000–1700 nm) region still hampers the success of NIR-II light-triggered phototheranostics. Herein, novel phototheranostic nanoparticles (PPN-NO NPs) were successfully prepared by coloading a cationic NIR-II CPs (PBC-co-PBF-NMe_3) and a NO donor (*S*-nitroso-*N*-acetylpenicillamine, SNAP) onto a 1:1 mixture of DSPE-PEG_{5000} and dimyristoylphosphatidylcholine (DMPC) for NIR-II FL and NIR-II photoacoustic (PA) imaging-guided low-temperature NIR-II photothermal therapy (PTT) and gas combination therapy for cancer treatment. A precise NIR-II FL dually enhanced design tactic was proposed herein by integrating flexible nonconjugated segments (C6) into the CPs backbone and incorporating quaternary ammonium salt cationic units into the CPs side chain, which considerably increased the radiative decay pathway, resulting in desirable NIR-II FL intensity and balanced NIR-II absorption and NIR PTT properties. The phototheranostic PPN-NO NPs exhibited distinguished NIR-II FL and PA imaging performance in tumor-bearing mice models. Furthermore, the low-temperature photothermal effect of PPN-NO NPs could initiate NO release upon 980 nm laser irradiation, efficiently suppressing tumor growth owing to the combination of low-temperature NIR-II PTT and NO gas therapy in vitro and in vivo.

Keywords Cationic NIR-II absorption conjugated polymer, Dually enhanced NIR-II fluorescence, Low-temperature NIR-II photothermal therapy, Gas therapy, Flexible nonconjugated segments

*Correspondence:
Pengfei Sun
iampfsun@njupt.edu.cn
Yingying Chen
chenyingying_zzu@163.com
Daifeng Li
lidaifeng@zzu.edu.cn
Full list of author information is available at the end of the article

© The Author(s) 2024. **Open Access** This article is licensed under a Creative Commons Attribution-NonCommercial-NoDerivatives 4.0 International License, which permits any non-commercial use, sharing, distribution and reproduction in any medium or format, as long as you give appropriate credit to the original author(s) and the source, provide a link to the Creative Commons licence, and indicate if you modified the licensed material. You do not have permission under this licence to share adapted material derived from this article or parts of it. The images or other third party material in this article are included in the article's Creative Commons licence, unless indicated otherwise in a credit line to the material. If material is not included in the article's Creative Commons licence and your intended use is not permitted by statutory regulation or exceeds the permitted use, you will need to obtain permission directly from the copyright holder. To view a copy of this licence, visit http://creativecommons.org/licenses/by-nc-nd/4.0/.

Graphical Abstract

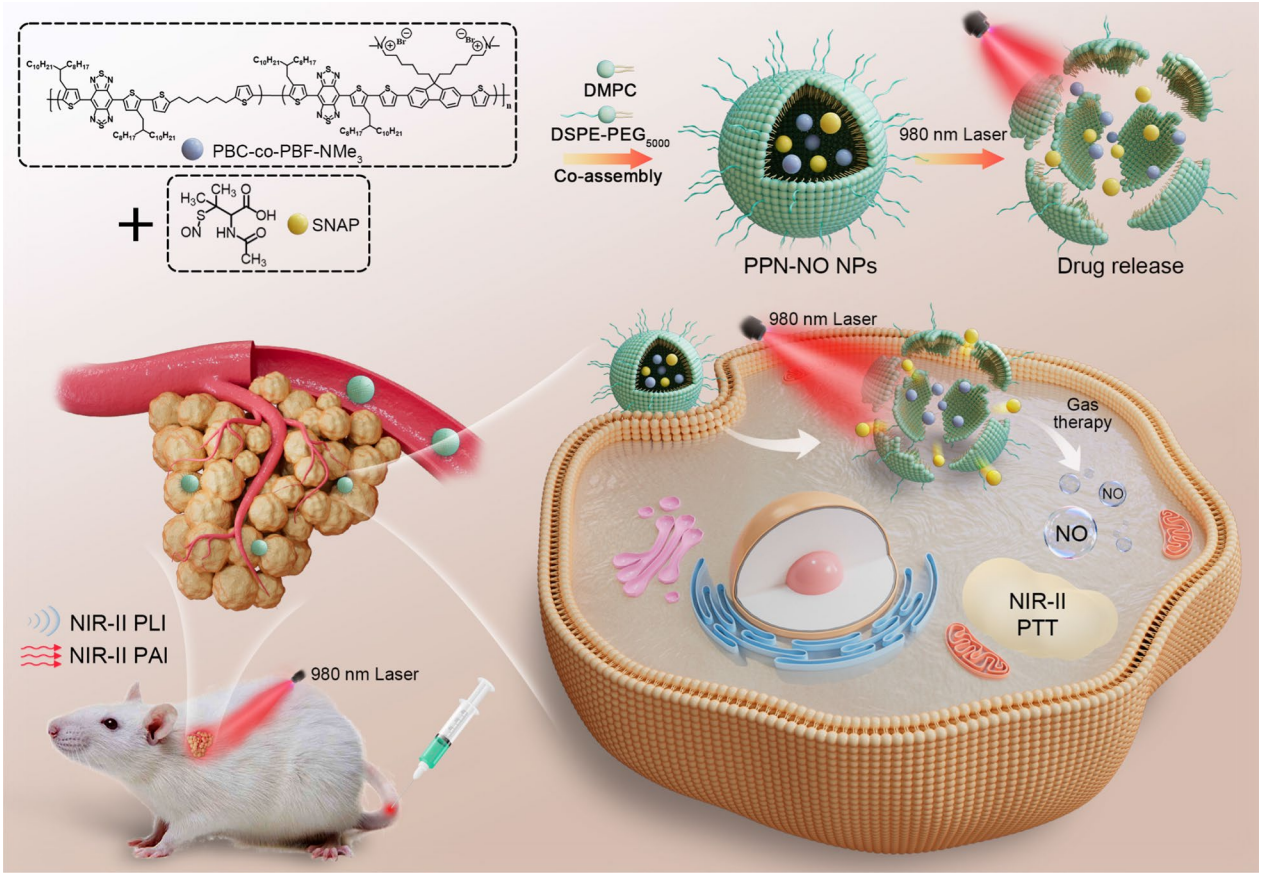

Introduction

Nowadays, cancer has caused great risks to public health. Traditional cancer treatment methods including chemotherapy and radiotherapy lead to high recurrence rates and drug resistance in patients [1, 2]. In recent years, near-infrared-II (NIR-II, 1000–1700 nm) light-excitation phototheranostics has been developed to enhance the effectiveness of anticancer treatments, because it allows deeper tissue penetration and a higher maximum permissible exposure density (1.0 W cm^{-2}) compared to near-infrared-I light-excitation phototheranostics [3–6]. For example, NIR-II photothermal therapy (PTT) effectively disrupts the integrity of cancer cells through photothermal conversion agents (PCAs) that generate hyperthermia (> 45 ℃) under light irradiation [7, 8]. Additionally, PCAs can convert absorbed photon energy into NIR-II fluorescence (FL) or NIR-II photoacoustic (PA) imaging signals for real-time and in situ treatment monitoring [9–13]. However, high temperatures reached during NIR-II PTT also cause unavoidable damage to tissues surrounding tumors, which can lead to inflammatory diseases. Therefore, low-temperature NIR-II PTT, which ablates cancer cells at temperatures below 45 ℃, may be an effective method to avoid damage to normal cells [14–20]. However, single low-temperature NIR-II PTT does not exhibit sufficient effectiveness and can lead to subsequent tumor recurrence. Therefore, it is crucial to combine low-temperature NIR-II PTT with other therapeutics [21–23]. Gas therapies (e.g., nitric oxide (NO) and carbon oxide (CO)), as enticing "green" therapeutic modalities, have garnered considerable attention in cancer treatment owing to their safety and negligible side effects [24–27]. For example, Cai et al. developed a CO gas/low-temperature PTT phototheranostic (PBPTV@mPEG(CO)) that integrates low-temperature PTT and a hydrogen peroxide (H_2O_2)-sensitive CO donor polymer for antitumor therapy [14]. Therefore, by loading thermal-sensitive gas therapy donors with PCAs, low-temperature NIR-II PTT/gas combination

phototheranostics can be developed to successfully achieve the tumor ablation effect.

To date, various NIR-II-absorbing agents, such as carbon nanotubes, gold nanomaterials, quantum dots, conjugated small molecule dyes, and donor–acceptor (D-A) structured conjugated polymers (CPs), have been extensively investigated for NIR-II phototheranostic. Among these diverse NIR-II-absorbing materials, organic CPs are advantageous in NIR-II FL/PA imaging-guided NIR-II PTT because of their reliable biosafety, strong intrinsic light-harvesting ability, high photothermal conversion, large Stokes shift, and good NIR-II FL [28–30]. Furthermore, the polymer skeletons of CPs can be flexibly modified to change their NIR-II optical and therapeutic properties. However, the NIR-II FL emits from currently available NIR-II-absorbing CPs is still very weak and do not meet the requirements of NIR-II FL/PA imaging-guided NIR-II PTT theranostics.

Therefore, it is necessary to develop CPs with high NIR-II absorbance and enhanced NIR-II emission using a simple and precise molecular engineering strategy. The incorporation of highly conjugated segments or coupling of strong electron donors/acceptors into the CPs backbone are common tactics to realize the NIR-II absorption wavelength. However, these design approaches hinder the radiative decay pathway for the dissipation of photon energy from the excited state and limit the NIR-II emission intensity of CPs. To address these problems, we proposed three strategies, namely, "electron acceptor density adjustment" [31], "weak-electron donor incorporation" [32], and "nonconjugated segment integration" [33] to adjust the structures of CPs backbones and promote their NIR-II FL. In addition, water-soluble NIR-II-absorbing CPs nanoparticles (NPs) exhibit further quenched NIR-II emissions because of the presence of strong intermolecular π-π stacking interactions in their aggregate state. Recently, some researchers have focused on enhancing the steric hindrance of polymer side chains or exploiting aggregation-induced emission luminogens (AIEgens) to block the FL quenching of water-soluble CPs and boost their NIR-II emission intensity [34–37]. Despite these progresses, the development of NIR-II-absorbing CPs with balanced NIR-II FL and photothermal performance via a convenient and versatile molecular engineering strategy remains challenging.

This study reports a type of multifunctional NIR-II PTT/gas cation phototheranostic (PPN-NO NPs) via coloading a heat-initiated NO donor (*S*-nitroso-*N*-acetylpenicillamine, SNAP) and a NIR-II-absorbing cationic CPs (PBC-co-PBF-NMe_3) for NIR-II FL/PA imaging-guided low-temperature NIR-II PTT and NO synergistic therapy of tumors. Herein, a precise dually enhanced molecular engineering tactic is demonstrated for constructing a cationic CPs with strong NIR-II absorbance, excellent NIR-II FL intensity, and satisfactory photothermal behavior upon 980 nm laser irradiation. In detail, flexible nonconjugated segments are tactfully incorporated into the CPs backbone to achieve high NIR-II absorption extinction coefficients by controlling the conjugation length of the polymer backbone. Quaternary ammonium salt cationic units are also modified into the side chain of the polymer skeleton to considerably reduce aggregation-caused FL quenching and improve the NIR-II emission intensity of CPs-based water-soluble NPs. PPN-NO NPs are prepared by coencapsulating PBC-co-PBF-NMe_3 and SNAP into a 1:1 mixture of DSPE-PEG_{5000} and dimyristoylphosphatidylcholine (DMPC). The as-prepared PPN-NO NPs can effectively generate toxic NO during the low-temperature NIR-II PTT process under 980 nm laser irradiation to trigger low-temperature NIR-II PTT/gas combination therapy (Scheme 1). PPN-NO NPs exhibit excellent performance during 980 nm laser-excited NIR-II FL/PA imaging and in vivo eradication of tumors.

Results and discussion

Synthesis and photophysical properties of non-conjugated segment-doped conjugated polymers

In our previous studies, we reported that the coupling of flexible nonconjugated segments with the CPs backbone is an effective strategy to control the length of the conjugated structure and enhance the NIR-II FL intensity of CPs. To construct NIR-II fluorescent CPs, two nonconjugated segment-doped CPs (PBC-co-PFC and PBC-co-PBF) were designed using different molar ratios of three units (electron acceptor, electron donor, and nonconjugated segments). This resulted in a varied distribution of nonconjugated segments within CPs; consequently, these two polymers have different lengths and compositions of conjugated segments. PBC-co-PFC and PBC-co-PBF polymers were synthesized via the standard Stille coupling polymerization (Scheme 2). In these two polymers, benzobisthiadiazole (BBT) was used as the electron acceptor unit in the CPs backbone to shift the absorption and FL wavelengths of CPs toward NIR-I and NIR-II regions, respectively. Furthermore, the bromine-functionalized bis(thiophene-2-yl)fluoren (TFT) derivative was used as electron donors and postmodification sites to increase the NIR-II FL of CPs in aqueous solutions. Furthermore, a nonconjugated segment 1,6-bis(thiophen-2-yl) hexane (C6) with flexible alkyl chain capabilities was added to the polymer backbone to finely tune the composition and length of conjugated segments. As shown in Scheme 1, the polycondensation of BBT, TFT, and C6 in a 1:1:2 molar feed ratio affords PBC-co-PFC. The flexible hexane chain has two conjugated segments T-BBT-T

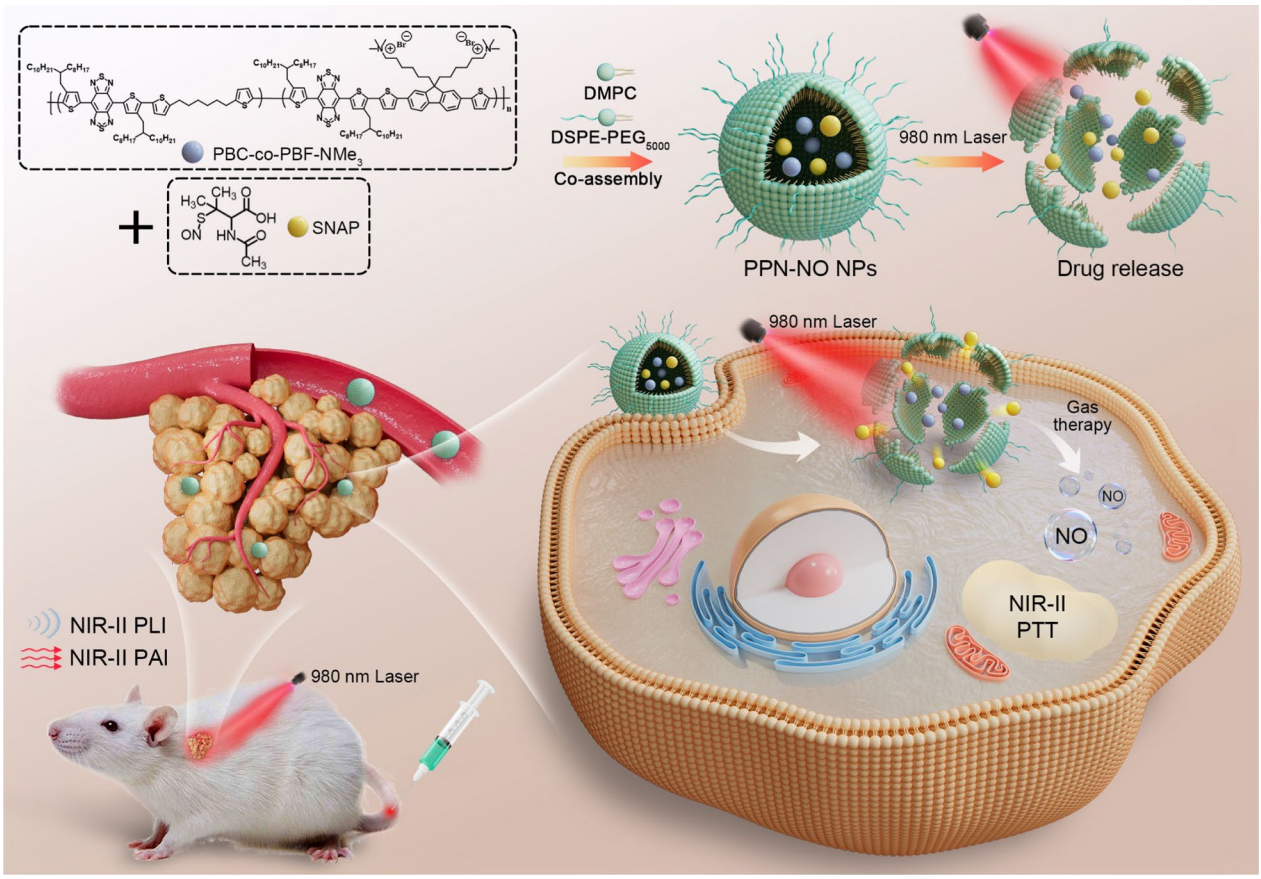

Scheme 1 Preparation of PPN-NO NPs and its application in NIR-II FL/NIR-II PA imaging-guided synergistic NIR-II PTT/NO gas therapy

and T-TFT-T (Scheme 2) in the polymer backbone of the PBC-co-PFC copolymer. However, using a 2:1:1 molar feed ratio of BBT, TFT, and C6, PBC-co-PBF was obtained, which comprised conjugated segments of BBT-TFT and T-BBT-T. PBF was prepared using a 1:1 ratio of BBT and TFT, where the repeating unit is BBT-TFT. The molecular structures of PBF, PBC-co-PBF, and PBC-co-PFC were confirmed via ^{1}H nuclear magnetic resonance (NMR) spectroscopy (Figures S1-S3). The number-average molecular weights (Mn) of the obtained polymers range from 10,000 to 15,000 g/mol with a polydispersity range of 1.5–1.6 (Figures S4-S6 and Table S1). PBF, PBC-co-PBF, and PBC-co-PFC exhibit excellent solubility in commonly used solvents such as tetrahydrofuran (THF) and dichloromethane (DCM).

To predict the photophysical properties of PBF, PBC-co-PBF, and PBC-co-PFC, density functional theory was used to analyze the electronic properties of the repeating conjugated segments in the backbones of these polymers. The highest occupied molecular orbital (HOMO) and lowest unoccupied molecular orbital (LUMO) levels of repeating units BBT-TFT, T-BBT-T, and T-TFT-T are shown in Fig. 1. The calculated energy bandgaps of BBT-TFT, T-BBT-T, and T-TFT-T are 1.34, 1.33, and 3.20 eV, respectively.

The photophysical properties of PBF, PBC-co-PBF, and PBC-co-PFC polymers were measured in THF. As shown in Fig. 2a, PBF exhibits strong absorption in the wavelength range of 600–900 nm. Meanwhile, PBC-co-PBF and PBC-co-PFC polymers exhibit broader wavelength absorption bands (700–1050 nm), extending even to the NIR-II region. The main absorption peaks of PBF, PBC-co-PBF, and PBC-co-PFC are 765 nm, 808 nm, and 831 nm, respectively. This indicates a clear redshift in the absorption wavelength when nonconjugated segments are introduced into the polymer backbone, probably because the repeating conjugated segment T-BBT-T in PBC-co-PBF and PBC-co-PFC has a lower bandgap than the repeating conjugated segment BBT-TFT in PBF, according to theoretical calculations shown in Fig. 1. Moreover, PBF, PBC-co-PBF, and PBC-co-PFC are completely soluble at a concentration of 0.2 mg mL^{-1} in THF (Figure S7). The extinction coefficients of PBF, PBC-co-PBF, and PBC-co-PFC at the main absorption peak

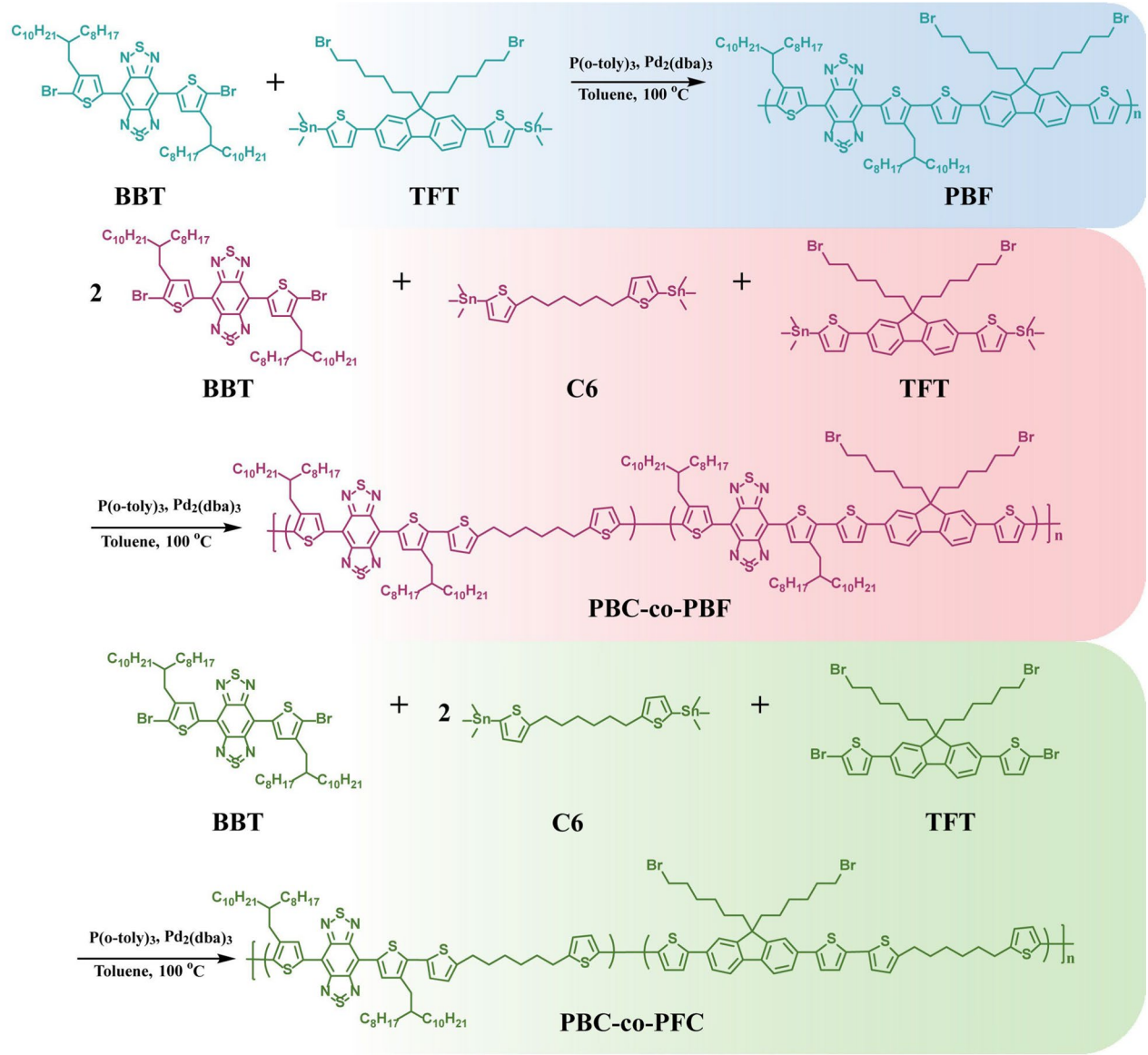

Scheme 2 Synthetic route of PBF, PBC-co-PBF, and PBC-co-PFC polymers

are 4.70, 15.22, and 9.84 L/g cm, respectively (Figs. 2b and S8). These results confirm that the incorporation of nonconjugated groups into the polymer backbone positively affects the polymer by improving its absorption wavelength and light-harvesting ability via enhancing its electron-donating ability and decreasing the bandgap of repeated conjugated segments.

More importantly, the NIR-II FL spectra of PBF, PBC-co-PBF, and PBC-co-PFC polymers were measured after 808 nm light excitation. As shown in Fig. 2c, the maximum NIR-II FL peaks of PBF, PBC-co-PBF, and PBC-co-PFC are observed at 990 nm, 1046 nm, and 1076 nm, respectively, with a weak shoulder peak at 1250 nm. In particular, the PBF solution exhibits a 1.9-fold higher FL intensity at the emission peak compared to PBC-co-PBF and PBC-co-PFC at the same concentration. It also has similar properties under the same 808 nm absorbance conditions (Fig. 2d and e). Furthermore, the NIR-II fluorescent images of PBF, PBC-co-PBF, and PBC-co-PFC in a THF solution were captured under a 1064 nm long pass filter. As shown in Fig. 2f, all three polymers show bright NIR-II fluorescent images and no obvious difference in their signal intensities is observed. This performance may be rationalized using their NIR-II FL spectra, which show similarly quantified integrated intensities of these polymers in the 900–1350 nm region (Figures S9 and S10).

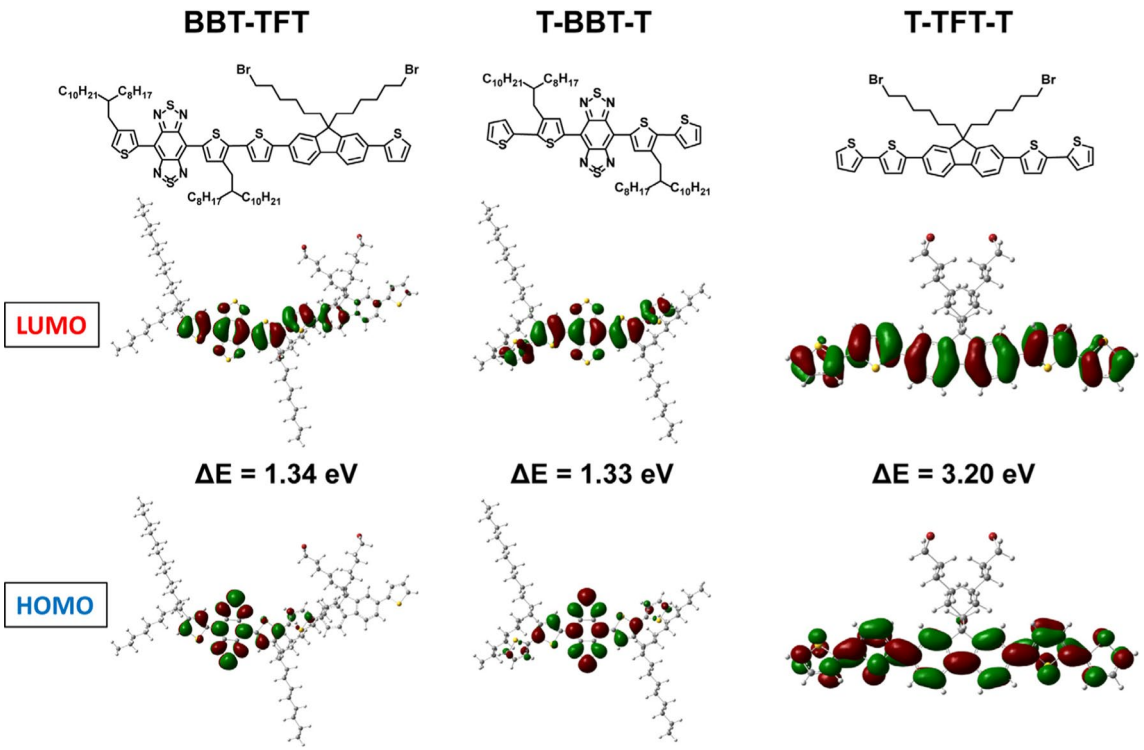

Fig. 1 Diagram of the LUMO and HOMO energy levels of repeating units BBT-TFT, T-BBT-T, and T-TFT-T

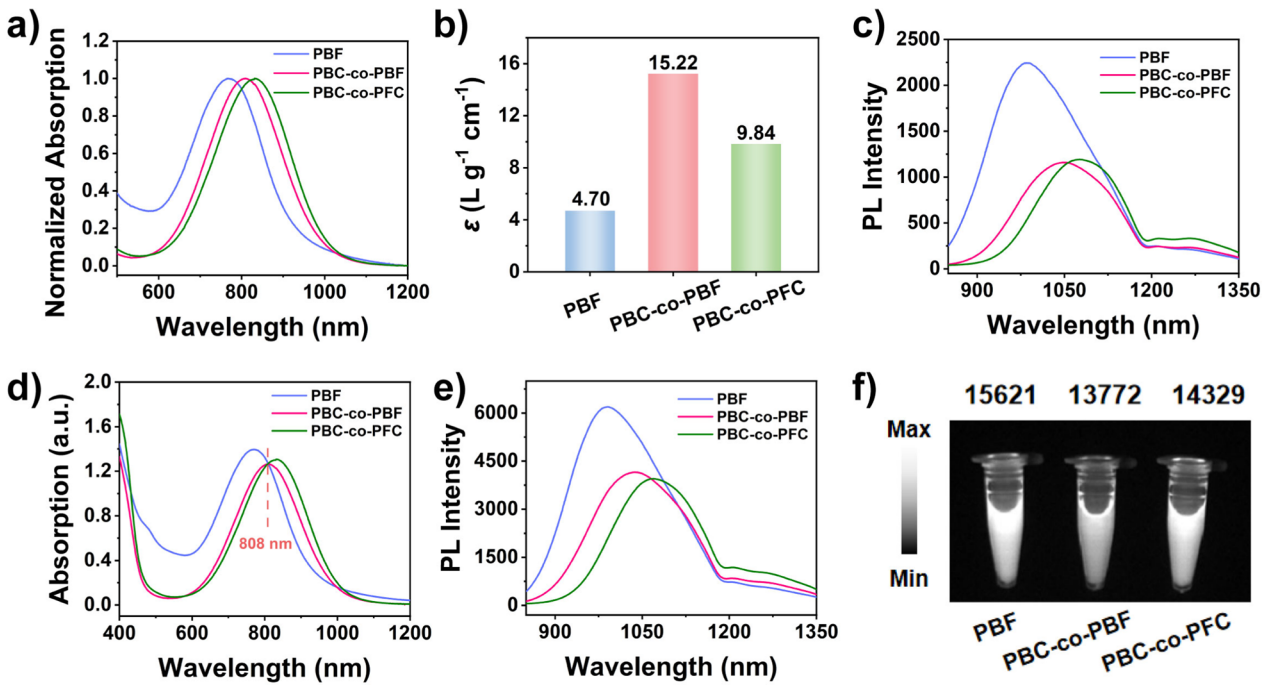

Fig. 2 **a** Normalized absorption spectra, **b** extinction coefficients at peak absorption, and **c** NIR-II FL spectra of PBF, PBC-co-PBF, and PBC-co-PFC polymers in a THF solution at concentration of 0.1 mg mL^{-1}. **d** Absorption and **e** NIR-II FL spectra of PBF, PBC-co-PBF, and PBC-co-PFC polymers in a THF solution with the same absorbance at 808 nm. **f** NIR-II fluorescent images of PBF, PBC-co-PBF, and PBC-co-PFC in a THF solution at concentration of 0.1 mg mL^{-1} (under 808 nm laser excitation and a 1064 nm LP filter)

Synthesis, photophysical properties, and NIR-II FL enhanced properties of cationic polymers

To endow hydrophobic CPs with water solubility for biomedical imaging and therapy applications, polymers need to self-assemble into NPs with amphiphilic copolymers via the nanoprecipitation method. However, typical CPs usually exhibit strong aggregation-caused quenching (ACQ), which results in the low NIR-II FL intensity of water-soluble NPs and hampers their applications in biological imaging. To address the problem of ACQ, three neutral polymers, PBF, PBC-co-PBF, and PBC-co-PFC, were further quaternizated into quaternary ammonium salt-modified cationic polymers, named PBF-NMe_3, PBC-co-PBF-NMe_3, and PBC-co-PFC-NMe_3, respectively (Fig. 3a and Scheme S1). The molecular structures of PBF-NMe_3, PBC-co-PBF-NMe_3, and PBC-co-PFC-NMe_3 were confirmed via ^{1}H NMR spectroscopy (Figures S11-S13). The photophysical properties of PBF-NMe_3, PBC-co-PBF-NMe_3, and PBC-co-PFC-NMe_3 in DCM were investigated. As shown in Fig. 3b, the color of polymer solutions changes from brown (PBF-NMe_3) to green (PBC-co-PFC-NMe_3) in DCM (0.2 mg mL^{-1}). As shown in Figs. 3c and S14, the maximum absorption of PBF-NMe_3, PBC-co-PBF-NMe_3, and PBC-co-PFC-NMe_3 is observed at 778 nm, 812 nm, and 830 nm, respectively. The FL spectrum of PBF-NMe_3, PBC-co-PBF-NMe_3, and PBC-co-PFC-NMe_3 excited under 808 nm light covers the NIR-II window, and the maximum emission peaks of PBF-NMe_3, PBC-co-PBF-NMe_3, and PBC-co-PFC-NMe_3 are observed at 988 nm, 1050 nm, and 1072 nm, respectively (Fig. 3d). In particular, the PBF-NMe_3 solution exhibits a 2.1-fold higher FL intensity at the emission peak compared to PBC-co-PFC-NMe_3 at the same concentration (Figure S15). It also has similar properties under the same 808 nm absorbance conditions (Figures S16-S18). These results are similar to those of its neutral CPs, implying that the photophysical properties of cationic polymers are not affected by the inclusion of quaternary ammonium salt pendants in the side chains.

Next, we encapsulated six polymers (PBF, PBC-co-PBF, and PBC-co-PFC, PBF-NMe_3, PBC-co-PBF-NMe_3, and PBC-co-PFC-NMe_3) with DMPC and investigated their NIR-II FL performance in an aqueous solution. First, as shown in Figures S19 and S20, the NPs are evenly dispersed in water. Dynamic light scattering (DLS) analysis shows that PBF NPs, PBC-co-PBF NPs, PBC-co-PFC NPs, PBF-NMe_3 NPs, PBC-co-PBF-NMe_3 NPs, and PBC-co-PFC-NMe_3 NPs have a particle size about 100 nm (Figures S21 and S22). PBF-NMe_3 NPs, PBC-co-PBF-NMe_3 NPs, and PBC-co-PFC-NMe_3 NPs are positively charged (Figure S23). As shown in Fig. 4a, b, S24, and S25, some differences are observed in the absorption

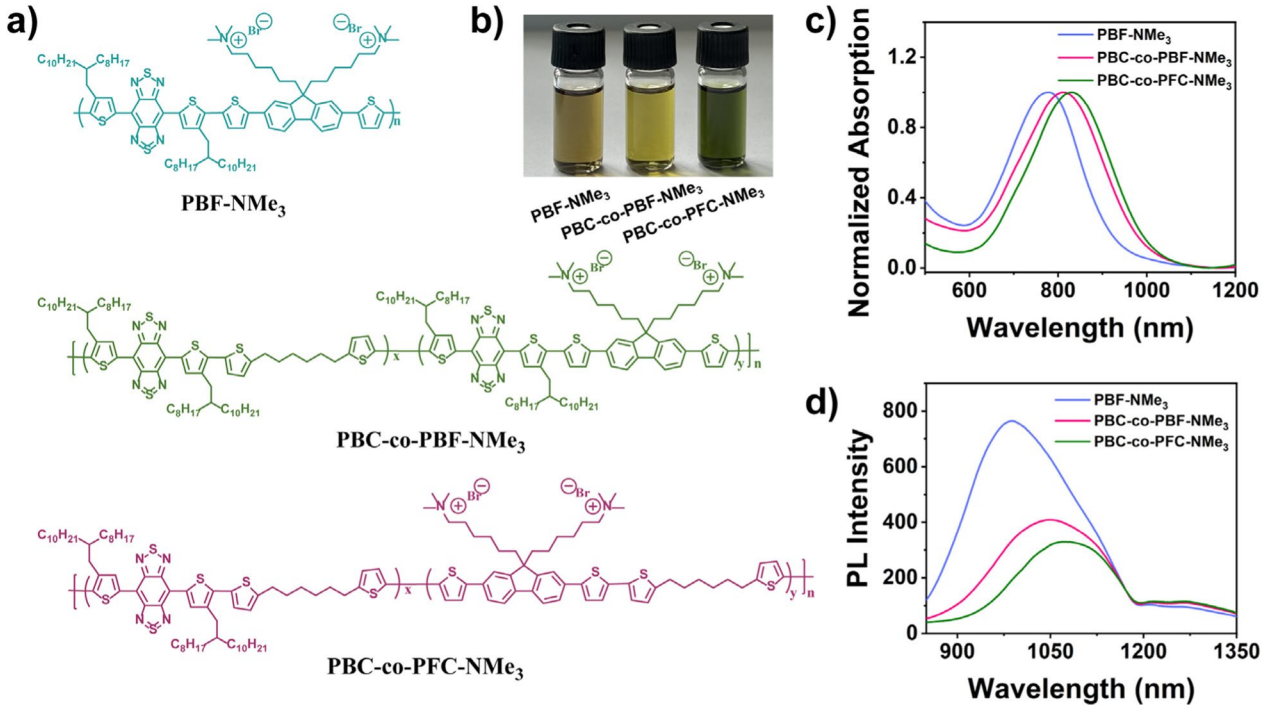

Fig. 3 **a** Chemical structures and **b** photographs of PBF-NMe_3, PBC-co-PBF-NMe_3, and PBC-co-PFC-NMe_3 in a DCM solution (0.2 mg mL^{-1}). **c** Normalized absorption spectra and **d** NIR-II FL spectra (under 808 nm laser excitation) of cationic polymers PBF-NMe_3, PBC-co-PBF-NMe_3, and PBC-co-PFC-NMe_3 at the same concentration

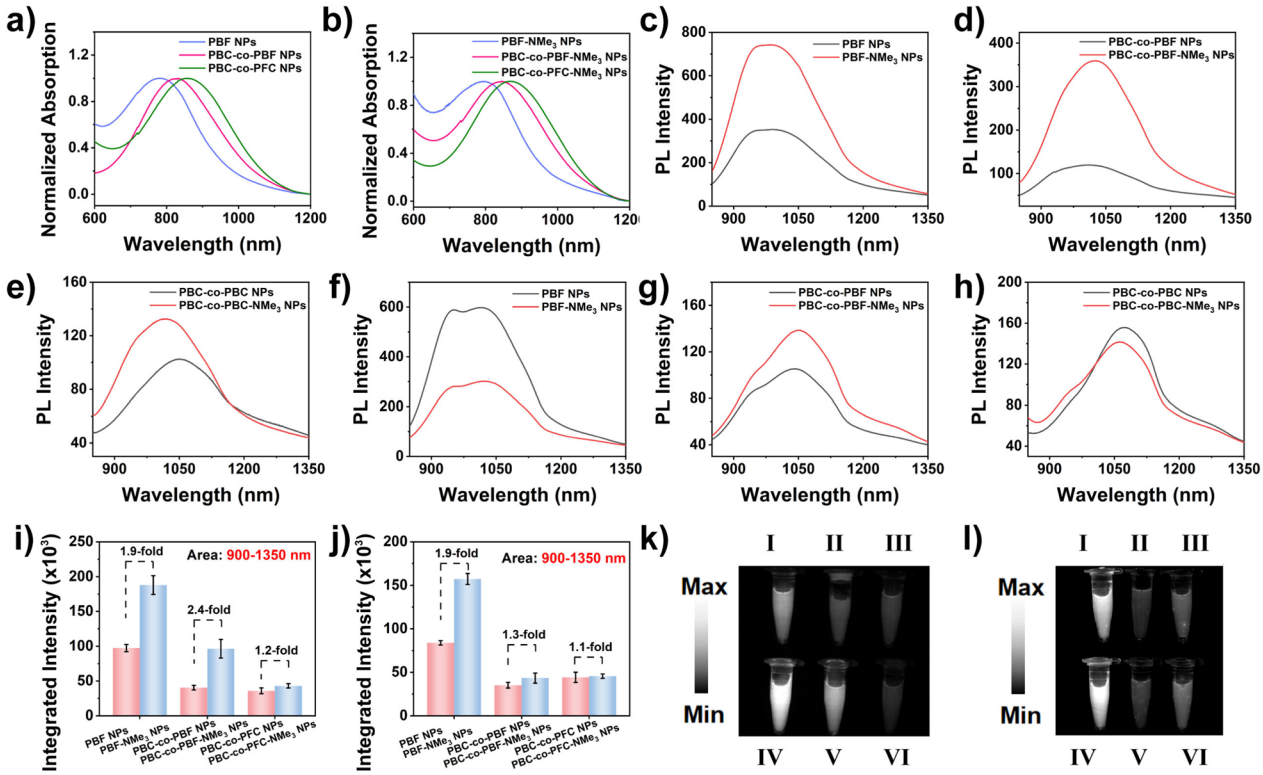

Fig. 4 Normalized absorption spectra of (**a**) neutral polymer-based PBF NPs, PBC-co-PBF NPs, and PBC-co-PFC NPs and (**b**) cationic polymer-based PBF-NMe_3 NPs, PBC-co-PBF-NMe_3 NPs, and PBC-co-PFC-NMe_3 NPs at the same concentration. NIR-II FL spectra of (**c**) PBF NPs and PBF-NMe_3 NPs, **d** PBC-co-PBF NPs and PBC-co-PBF-NMe_3 NPs, and (**e**) PBC-co-PFC NPs and PBC-co-PFC-NMe_3 NPs in an aqueous solution under 808 nm laser excitation at a concentration of 0.1 mg mL^{-1}. NIR-II FL spectra of (**f**) PBF NPs and PBF-NMe_3 NPs, **g** PBC-co-PBF NPs and PBC-co-PBF-NMe_3 NPs, and **h** PBC-co-PFC NPs and PBC-co-PFC-NMe_3 NPs in an aqueous solution under 808 nm laser excitation with the same absorbance. **i** Corresponding quantified FL integrated intensities (range = 900–1350 nm) of (**c**), (**d**), and (**e**). **j** Corresponding quantified FL integrated intensities (range = 900–1350 nm) of (**f**), (**g**), and (**h**). NIR-II fluorescent images of PBF-NMe_3 NPs and PBF NPs, PBC-co-PBF-NMe_3 NPs and PBC-co-PBF NPs, and PBC-co-PFC-NMe_3 NPs and PBC-co-PFC NPs in an aqueous solution (**k**) at a concentration of 0.1 mg mL^{-1} and (**l**) with the same absorbance at 808 nm (under 808 nm laser excitation and with a 1064 nm LP filter). (I: PBF NPs, II: PBC-co-PBF NPs, III: PBC-co-PFC NPs, IV: PBF-NMe_3 NPs, V: PBC-co-PBF-NMe_3 NPs, VI: PBC-co-PFC-NMe_3 NPs)

spectra of cationic and neutral polymer-based NPs. The main absorption peaks of cationic CPs-based NPs are observed at 790 nm (PBF-NMe_3 NPs), 844 nm (PBC-co-PBF-NMe_3 NPs), and 870 nm (PBC-co-PFC-NMe_3 NPs), respectively, indicating that quaternary ammonium modification redshifts the absorption wavelength compared to PBF NPs (784 nm), PBC-co-PBF NPs (832 nm), and PBC-co-PFC NPs (854 nm), respectively.

To investigate the fluorescence anti-quenching properties of cationic CPs when they self-assemble with DMPC in water, we recorded the NIR-II fluorescence spectra of six prepared water-soluble nanoparticles. As shown in Fig. 4c, PBF-NMe_3 NPs with quaternary ammonium on all conjugated sites exhibit a 1.9 times higher FL intensity than PBF NPs. However, the FL intensity of PBC-co-PFC-NMe_3 NPs is only 1.2 times higher than that of PBC-co-PFC NPs (Fig. 4d). In addition, the FL intensity of PBC-co-PBF-NMe_3 NPs is 2.4-fold higher than that of PBC-co-PBF NPs (Fig. 4e). These results indicate that the NIR-II FL intensity of cationic CPs-based NPs is stronger than that of neutral CPs-based NPs at the same concentration. Notably, PBC-co-PBF-NMe_3, containing BBT-TFT and T-BBT-T conjugated segments, exhibits a considerably enhanced FL intensity compared to that of PBC-co-PFC-NMe_3 with T-BBT-T and T-TFT-T segments. Then, the NIR-II FL imaging capabilities of these NPs were evaluated. As shown in Figs. 4k and S26, PBC-co-PBF-NMe_3 NPs also exhibit the strongest FL enhancement performance. A comparison of the chemical structures in PBC-co-PBF-NMe_3 and PBC-co-PFC-NMe_3 shows that quaternary ammonium is located within BBT-related segments (BBT-TFT) of PBC-co-PBF-NMe_3, however, quaternary ammonium is dispersed among T-TFT-T segments in PBC-co-PFC-NMe_3. Therefore, it is deduced that the enhancement in the FL intensity of cationic CPs is associated with the position of quaternary

ammonium within the conjugated segment. The modification of quaternary ammonium at the electron acceptor site may result in looser intrachain stacking, which benefits the anti-quenching properties of cationic CPs and increases the NIR-II FL intensity of cationic CPs.

To further understand the FL enhancement, we studied the NIR-II FL spectra and imaging of NPs at the same 808 nm absorption wavelength (Figs. 4f–h, j, S27, and S28). PBC-co-PBF-NMe_3 NPs exhibit the highest NIR-II FL intensity and the strongest FL enhancement performance among all synthesized NPs. These results provide additional evidence for the aforementioned conclusion. Next, the NIR-II photothermal properties of these obtained water-soluble NPs were evaluated. As shown in Figures S29-S31, the temperature of PBC-co-PBF-NMe_3 NPs is 47.9 ℃ after 5 min of irradiation using a 980 nm laser (1.0 W cm^{-2}). However, under the same conditions, the temperatures of PBF-NMe_3 NPs and PBC-co-PFC-NMe_3 are slightly lower (41.2 ℃ and 43.7 ℃, respectively), probably owing to their relatively weaker absorption at 980 nm. These results suggest that changes in the distribution of nonconjugated groups in the polymer backbone may afford CPs-based NPs with extended absorption in the NIR-II region, enhanced NIR-II FL, and strong NIR-II photothermal effects. This may be an effective molecular engineering strategy for designing NIR-II phototheranostics.

Preparation and characterization of PPN-NO NPs

Based on the above properties, PBC-co-PBF-NMe_3 was selected for biological applications owing to its satisfactory absorption in the NIR region, high NIR-II FL intensity after assembly with DMPC, and desirable photothermal properties under 980 nm laser irradiation. As shown in Fig. 5a, we prepared a 980 nm laser-triggered NIR-II PTT/NO gas synergistic therapy phototheranostics using PBC-co-PBF-NMe_3. PPN-NO NPs are prepared by coencapsulating PBC-co-PBF-NMe_3 and heat-initiated SNAP as an NO donor in a 1:1 mixture of DSPE-PEG_{5000} and DMPC. The loading efficiency of SNAP in PPN-NO NPs is 3.11%, according to the standard curve and UV absorption curve during the illumination process (Figure S32). The DLS results in Fig. 5b show that PPN-NO NPs have an average hydrodynamic diameter (D_h) of 96.2 nm and with a low polydispersity index of 0.12. The TEM images show that PPN-NO NPs have a spherical morphology (Fig. 5c). After 10 days of preservation of PPN-NO NPs in a phosphate buffered saline (PBS) solution containing 10% fetal bovine serum and Dulbecco's Modified Eagle medium, there was little change in D_h (Figures S33 and S34). The EDS element mapping of PPN-NO NPs shows N and O are well distributed across NPs, demonstrating successful SNAP loading (Fig. 5d). As shown in Figs. 5e and S35, the absorption spectrum of PPN-NO NPs ranges from 700 to 1050 nm. Figure 5f and g show that PPN-NO NPs exhibit a strong NIR-II emission band and NIR-II fluorescent images upon excitation at 808 nm and 980 nm, respectively. Unlike IR1061, the NIR-II FL intensity of PPN-NO NPs remains nearly constant for 50 min (808 nm, 1.0 W cm^{-2}), indicating that PPN-NO NPs are photostable (Figure S36).

As shown in Figs. 5h and S37, the temperature of PPN-NO NPs (at a concentration of 0.2 mg mL^{-1}) increases to 47.5 ℃ upon 980 nm laser (1.0 W cm^{-2}) irradiation for 5 min, which is high enough to effectively eliminate cancer cells. The photothermal conversion efficiency of PPN-NO NPs is 21.37%. As shown in Fig. 5i, the temperature of the aqueous PPN-NO NPs solution increases with an increase in its concentration. The heat generation performance of PPN-NO NPs is negligibly attenuated after five on−off irradiation cycles, demonstrating their excellent photothermal stability (Fig. 5j). In addition, PPN-NO NPs exhibit strong PA signals under 980 nm laser excitation (Fig. 5k). The NIR-II PA signals intensity of PPN-NO NPs demonstrate an excellent linear relation with the NPs concentration (Figure S38). The heat generated from the photothermal performance of PPN-NO NPs can trigger the decomposition of SNAP and induce NO generation. Therefore, we further studied the NO releasing efficiency of PPN-NO NPs using the Griess agent, which is a typical NO sensor with a responsive absorption of 540 nm. Interestingly, a noticeable increase in the 540 nm absorption is observed after the 980 nm laser irradiation of PPN-NO NPs (1.0 W cm^{-2}) for 10 min, indicating the successful NO release from PPN-NO NPs via the NIR-II photothermal effect (Fig. 5l). The NO release from PPN-NO NPs reaches a plateau after 40 min of irradiation, and the cumulative NO release ratio is about 60% (Figure S32).

In vitro antitumor activity of PPN-NO NPs

First, the uptake of PPN-NO NPs was observed via flow cytometry and confocal laser scanning microscopy (CLSM), which showed that PPN-NO NPs are ingested in large quantities within 4 h (Figure S39). Encouraged by their NIR-II photothermal performance and light-responsive NO release, we investigated the in vitro antitumor efficacy of PPN-NO NPs using 4T1 cancer cells as a model. First, we examined the intracellular NO generation in 4T1 cancer cells using CLSM with commercial DAF-FM DA as a fluorescent probe. As shown in Fig. 6a, the CLSM images show the bright green FL signals of DAF-FM DA in 4T1 cells treated with PPN-NO NPs and 10 min of 980 nm laser irradiation (1.0 W cm^{-2}), demonstrating elevated NO levels in 4T1 cells. Second, we studied the antitumor effect of PPN-NO NPs as an ideal

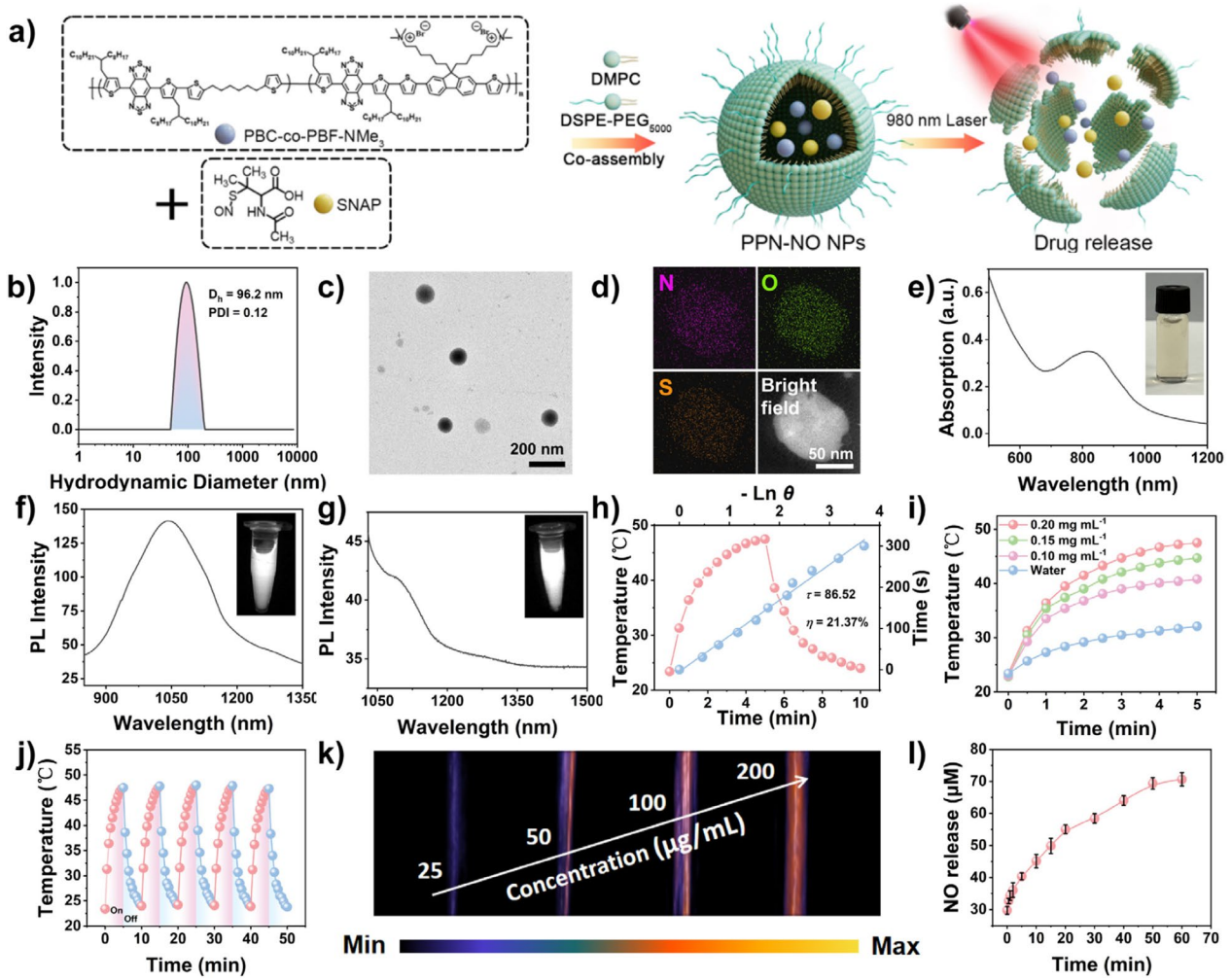

Fig. 5 **a** Schematic of the preparation of PPN-NO NPs. **b** Average hydrodynamic diameters (D_h), **c** transmission electron microscopy (TEM) images (scale bar = 200 nm), and **d** TEM energy-dispersive X-ray spectroscopy (EDS) element mapping of PPN-NO NPs (scale bar = 50 nm). **e** Absorption spectra of PPN-NO NPs in water. Inset: Photograph of PPN-NO NPs solutions. NIR-II FL spectra and NIR-II FL images of PPN-NO NPs under **f** 808 nm and **g** 980 nm laser excitation. Inset: NIR-II fluorescent images of PPN-NO NPs. **h** Photothermal performance of PPN-NO NPs (0.2 mg mL^{-1}) upon excitation using a 980 nm laser (1.0 W cm^{-2}) and linear correlation of the cooling times *vs.* negative natural logarithm of driving force temperatures for PPN-NO NPs. **i** Photothermal heating curves of water and PPN-NO NPs at concentrations of 0.20, 0.15, and 0.10 mg mL^{-1} under 980 nm laser irradiation (1.0 W cm^{-2}). **j** Photothermal stability of aqueous PPN-NO NPs solution during five on/off irradiation cycles using a 980 nm laser at a power density of 1.0 W cm^{-2}. **k** PA images of PPN-NO NPs at various concentrations under 980 nm laser excitation. **l** Release curve of NO in PPN-NO NPs upon 980 nm laser irradiation (1.0 W cm^{-2}) (n = 3). Data are represented as mean ± standard deviation (SD)

NIR-II PTT/NO phototheranostic agent using MTT assays. Figure 6b shows that the survival rates of cells in the PBS, PPN-NO NPs, PPN NPs+980 nm laser, and PPN-NO NPs+980 nm laser groups are 96%, 93%, 64%, and 13%, respectively. These results demonstrate that the synergistic NIR-II PTT/NO therapy based on PPN-NO NPs can effectively kill 4T1 cancer cells. A live/dead cancer cell viability assay was also performed to evaluate the in vitro antitumor efficacy of PPN-NO NPs. Living and dead cells were stained with Calcein AM (green FL for living) and propidium iodide (red FL for dead), respectively. The cells in the PPN-NO NPs+980 nm laser group exhibit almost completely red-stained FL (Fig. 6c), which further manifesting efficiently damage mediated by synergistic NIR-II PTT/NO therapy of PPN-NO NPs. However, fewer dead cells are observed in the individual NIR-II PTT and NO therapy group and control groups (cells treated by PPN-NO NPs only or PPN NPs+980 nm laser). Finally, the same results are obtained via flow cytometry analysis. As shown in Fig. 6d, the cell apoptosis rate is the highest (85.90%) in the PPN-NO NPs+980 nm laser group, and it exceeds that of the individual PPN

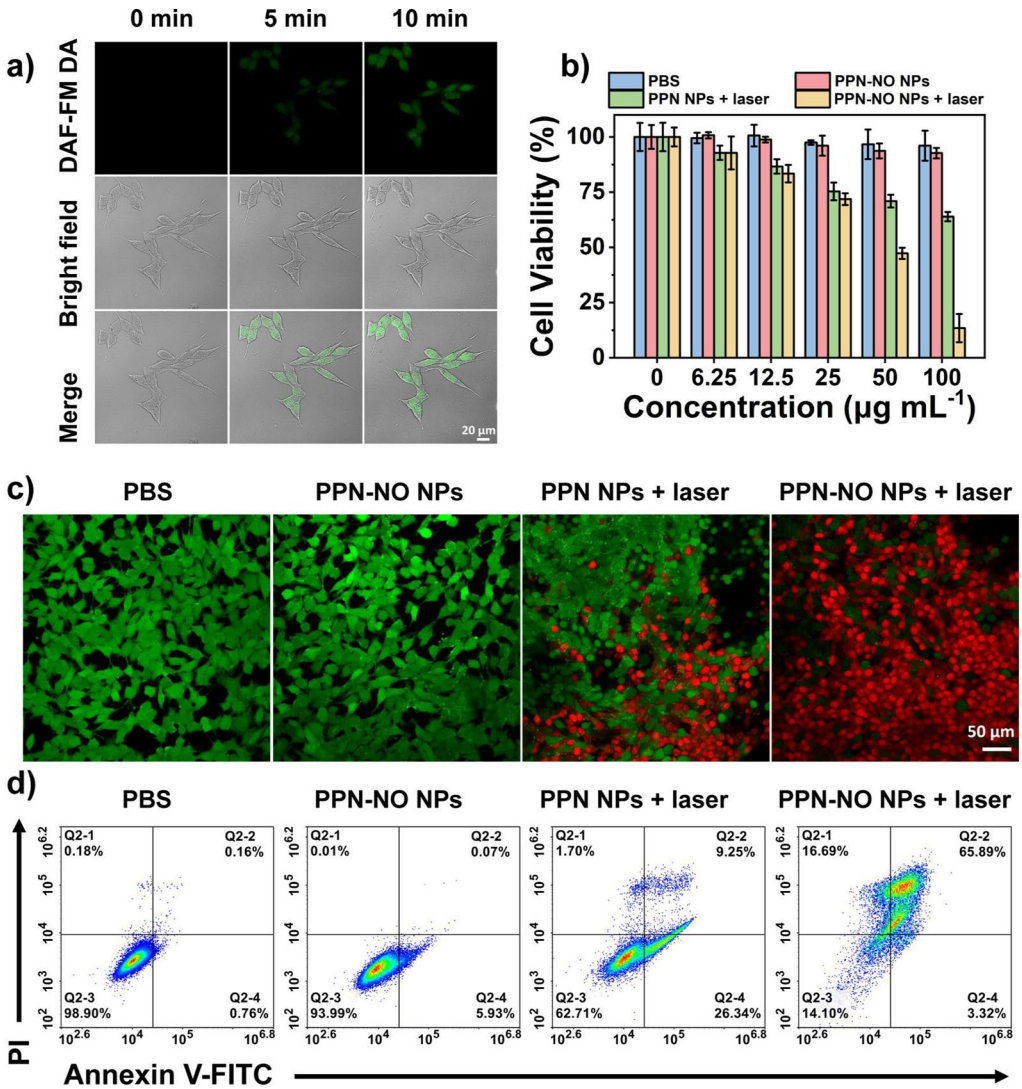

Fig. 6 **a** CLSM images of the NO release behavior of PPN-NO NPs detected based on the FL intensity of DAF-FM DA (green) after 980 nm laser irradiation (scale bar = 20 μm) **b** Viability of 4T1 cells after receiving different treatments (PBS, PPN-NO NPs, PPN NPs + 980 nm laser, and PPN-NO NPs + 980 nm laser) at different concentrations (n = 5). **c** Live/dead staining (scale bar = 50 μm) and (**d**) flow cytometry of 4T1 cells after various treatments (PBS, PPN-NO NPs, PPN NPs + 980 nm laser, and PPN-NO NPs + 980 nm laser). Data are represented as mean ± standard deviation (SD)

NPs+980 nm laser group (37.29%), demonstrating the superior cytotoxicity of the combination NIR-II PTT/NO therapies.

In vivo antitumor activity of PPN-NO NPs

Encouraged by the in vitro synergistic therapeutic results, we further studied the feasibility of PPN-NO NPs for NIR-II FL/PA imaging-guided NIR-II PTT/NO combination therapy in 4T1 tumor-bearing mice. First, we captured the 980 nm laser-excited NIR-II FL and NIR-II PA imaging spectra after the intravenous injection of PPN-NO NPs into model mice. As shown in Fig. 7a and c, the NIR-II FL and NIR-II PA signals in tumor sites can be observed at the infection site after 8 h postinjection of PPN-NO NPs. Meanwhile, the intensity of NIR-II FL and NIR-II PA imaging signals in the tumor region increases and reaches the maximum at 24 h (Fig. 7b and d), where the imaging intensities are 3.1- and 15.3-fold higher than that before injection, respectively, suggesting the prominent tumor-accumulation ability of PPN-NO NPs is motivated by the enhanced permeability and retention effect. After 24 h postinjection, the ex vivo NIR-II FL and NIR-II PA images of the tumor, liver, spleen, lung, and kidney of model mice were assessed. As shown in Figures S40 and S41, the imaging signal in the tumor region appears brighter than that in other tissues, which is

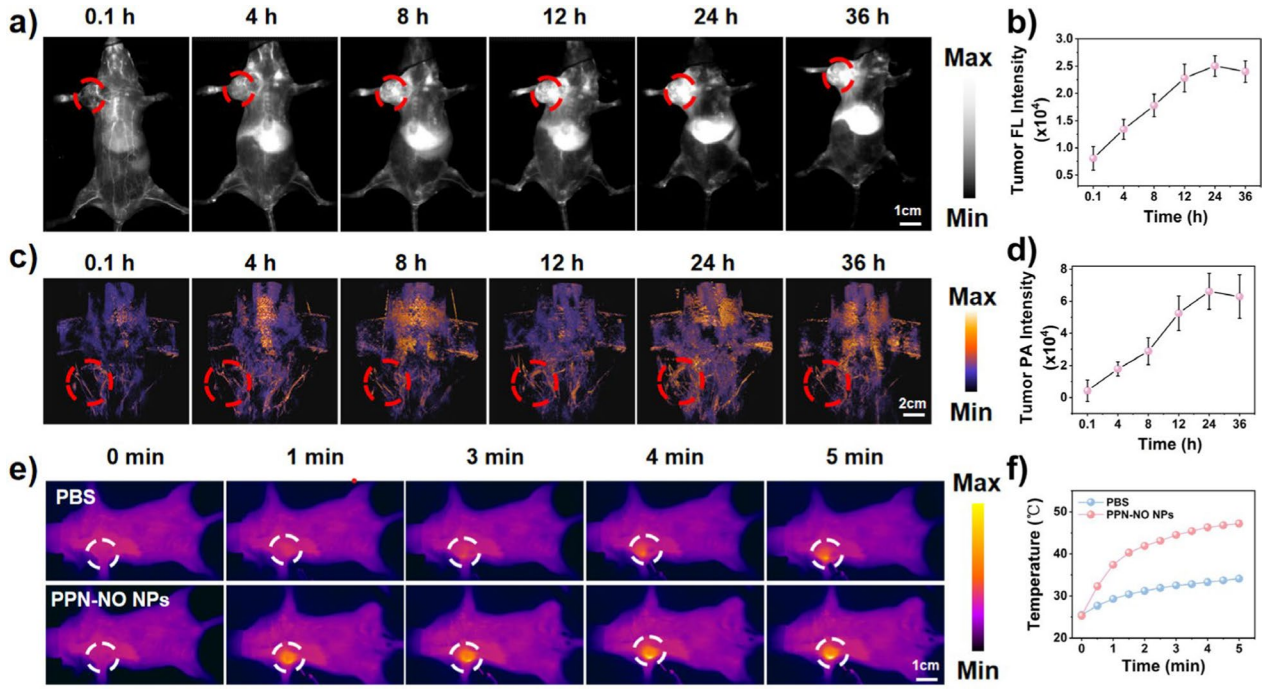

Fig. 7 In vivo NIR-II (**a**) FL and (**c**) PA images of 4T1 tumor-bearing mice (intravenous injection of PPN-NO NPs, 2.0 mg mL^{-1}, 150 μL). Corresponding quantification of NIR-II (**b**) FL and (**d**) PA signals of the tumor at different monitoring times (n = 3). **e** Infrared photothermal images and (**f**) corresponding temperature variations at tumor sites after receiving treatments of PBS or PPN-NO NPs (2.0 mg mL^{-1}, 150 μL) under 980 nm laser irradiation (1.0 W cm^{-2}, 5 min) (n = 3). Data represent mean ± standard deviation (SD)

beneficial for the subsequent in vivo therapy against the tumor.

4T1 tumor-bearing mice were randomly divided into two groups, PBS and PPN-NO NPs + 980 nm laser groups. After 24 h postinjection intravenous injection of NPs, we performed 980 nm laser irradiation on the tumor region of the mice in the PBS and PPN-NO NPs groups for in vivo photothermal evaluation. As shown in Figs. 7e and f, the temperature at the tumor site rapidly increases to 47.2 ℃ for the PPN-NO NPs + 980 nm laser groups after 5 min irradiation (980 nm, 1.0 W cm^{-2}), which is high enough for killing tumor tissues and initiate NO generation, ensuring the NIR-II PTT/NO combination therapy.

After different treatments, we measured the tumor volume within 15 days, as shown in Fig. 8a. A steady increase is observed in the tumor in the PPN-NO NPs groups with time, and the tumor growth shows a 10.4-fold increase, suggesting that PPN-NO NPs alone have little inhibitory influence on tumor growth. In stark contrast, the tumor growth in the treatment groups, including PPN NPs + 980 nm laser and PPN-NO NPs + 980 nm laser groups, shows 7.4- and 1.4-fold increase, respectively, indicating that combination therapy can inhibit tumor growth (Fig. 8a). As expected, the tumor growth-inhibition performance of PPN-NO NPs + 980 nm laser is better than that of PPN NPs + 980 nm laser owing to the combination of NIR-II PTT and NO. During the whole treatment period, no treatment-caused virtual changes in the body weight are observed, indicating minimal side effects of PPN NPs on living mice (Figure S42). After 15 days of treatment, the tumors were collected (Fig. 8b). The tumor weight is considerably lower in the PPN-NO NPs + 980 nm laser group (0.16 g) compared to the control (1.21 g), PPN NPs (1.17 g), and PPN NPs + 980 nm laser groups (0.82 g). These results further confirm the excellent in vivo NIR-II PTT/NO combination therapy performance of PPN-NO NPs with the aid of 980 nm laser irradiation (Fig. 8c).

Next, tumor tissues were further assessed via hematoxylin and eosin (H&E) staining, terminal deoxynucleotidyl transferase dUTP nick-end labeling (TUNEL) staining, and immunohistochemistry (Ki-67) immunofluorescence staining after 15 days of treatment (Fig. 8d). H&E and TUNEL staining results from the PPN-NO NPs + 980 nm laser group exhibit considerable cell necrosis and remarkable abnormality of tumor cells, suggesting a favorable antitumor ability. However, little damage to the tumor tissues is observed in the control and PPN NPs groups. Furthermore, the Ki-67 immunofluorescence staining analysis indicates that the PPN-NO NPs + 980 nm laser group possesses

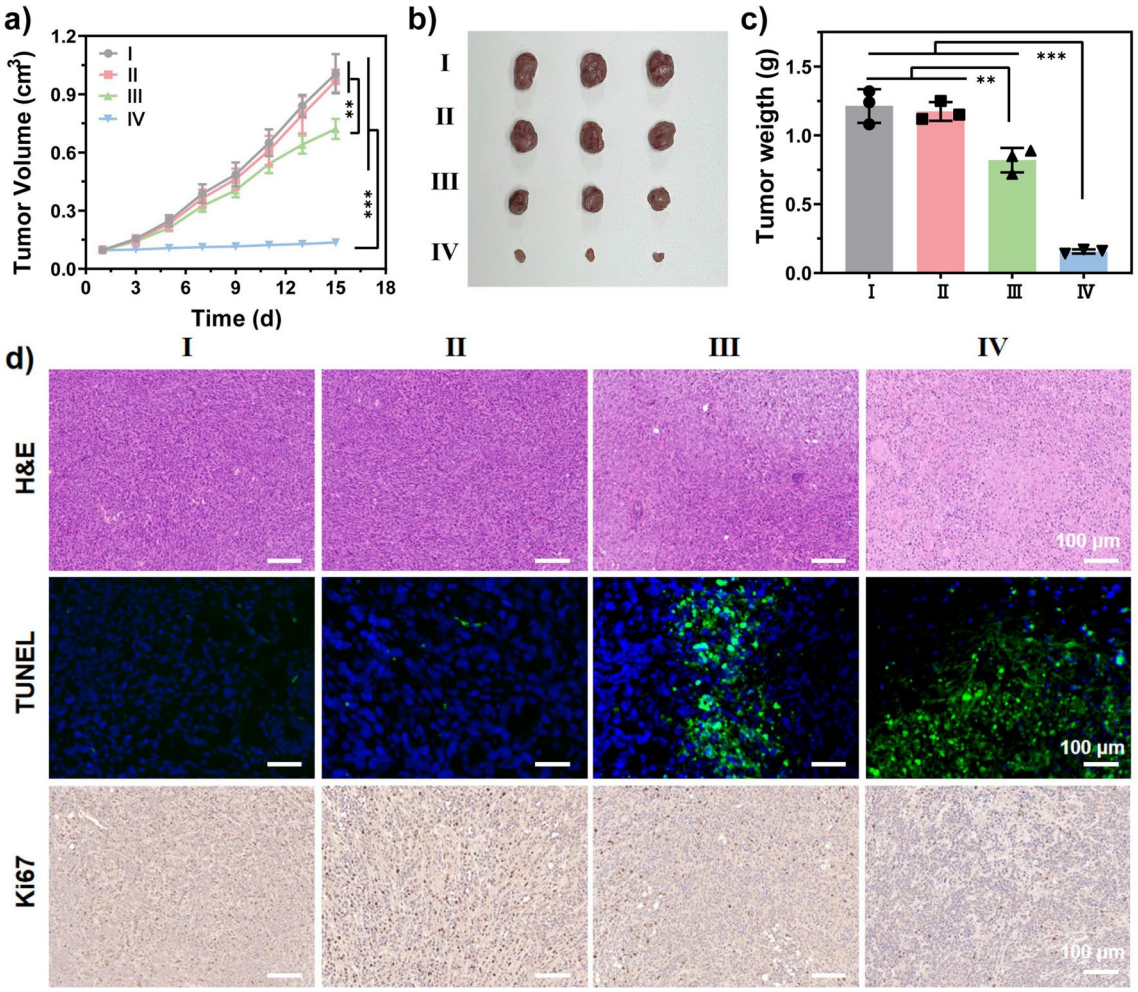

Fig. 8 **a** Changes in the tumor volume in the 4T1 tumor-bearing mice in different groups during the 15-day study after various treatments (n = 3). **b** Tumor images and (**c**) weights after 15-day treatment (n = 3). **d** The H&E, TUNEL, and Ki-67 immunofluorescence staining images of the tumor after 15-day treatment (scale bar = 100 μm). (I: PBS, II: PPN-NO NPs, III: PPN NPs+laser, IV: PPN-NO NPs+laser (1.0 W cm^{-2})). Data are represented as mean ± standard deviation (SD). (No significance: n.s., $*p < 0.05$, $**p < 0.01$, $***p < 0.001$)

a lower number of proliferating tumor cells compared to other groups, which is consistent with H&E and TUNEL staining results. The results from in vivo treatments highlight the excellent antitumor efficacy of PPN-NO NPs by a combination of NIR-II PTT and NO gas therapy.

The in vivo biosafety of PPN-NO NPs was further evaluated by analyzing the blood biochemical indexes. The parameters of biochemical indexes, including liver and kidney function markers, remain within the normal range in the PPN-NO NPs+ 980 nm laser group 15 days post-treatment and show no apparent difference compared to other control groups (Figure S43a), demonstrating the good biological security of PPN-NO NPs. The H&E staining images of major organs (heart, liver, spleen, lung, and kidney) resected from the PPN-NO NPs+ 980 nm laser group show no signs of infection or inflammation, further supporting the low systemic toxicity of PPN-NO NPs (Figure S43b).

Conclusion

Herein, a multifunctional gas/phototheranostic (PPN-NO NPs) was developed for NIR-II FL/PA imaging-guided low-temperature NIR-II PTT and NO gas combination therapy for tumor theranostics. A precise dually enhanced engineering strategy combining flexible nonconjugated segments and quaternary ammonium salt cationic units into the CPs backbone and side chain was developed, which allowed the flexible tuning of NIR-II absorption and photothermal conversion capacity and boosted the NIR-II FL properties of PBC-co-PBF-NMe_3. PPN-NO NPs were engineered by

encapsulating PBC-co-PBF-NMe_3 and SNAP in a 1:1 mixture of DSPE-PEG_{5000} and DMPC. PPN-NO NPs not only exhibit low-temperature photothermal behavior but also enable the controlled release of NO to initiate gas therapy upon 980 nm laser irradiation. In vivo experiments showed that PPN-NO NPs possess prominent NIR-II FL/PA imaging efficiency and remarkable NIR-II PTT/NO synergistic ablation capability towards tumor.

Supplementary Information

The online version contains supplementary material available at https://doi.org/10.1186/s12951-024-02741-9.

Additional file 1. Figure S1-S3 and Figure S11-S13. Nuclear magnetic resonance spectra. Figure S4-S6. The gel permeation chromatography spectra. Figure S7-S10. Solution photograph, extinction coefficient, and fluorescence integral area. Figure S14-S43. Extinction coefficient, fluorescence integral area, absorption, solution photo, average hydrodynamic diameter, zeta potential, photothermal curve, nanoparticle stability, cell uptake, NIR-II fluorescence imaging in vitro, NIR-II photoacoustic imaging in vitro and biocompatibility.

Acknowledgements
We are grateful for financially support from Young Elite Scientists Sponsorship Program by CAST (2023QNRC001, Daifeng Li), Youth Talent Promotion Project of Henan Province (2023HYTP042, Daifeng Li), and Key Projects of Medical Science and Technology of Henan Province (SBGJ202102116, Daifeng Li). The authors acknowledge assistance with the access to analytic instruments from the Translational Medicine Center at the First Affiliated Hospital of Zhengzhou University.

Author contributions
Daifeng Li, Yingying Chen and Pengfei Sun conceived the project and designed the experiments. Kexi Liu, Danni Hu and Peng Cheng performed the spectral and cell experiments and analyzed the data. Kexi Liu, Liuliang He and Zhichao Wang performed the animal experiments. Daifeng Li and Pengfei Sun supervised the project. Daifeng Li, Yingying Chen and Pengfei Sun helped with the revision of this manuscript. All of the authors were involved in the analysis and interpretation of data.

Funding
Key Projects of Medical Science and Technology of Henan Province, SBGJ202102116, Young Elite Scientists Sponsorship Program by CAST, 2023QNRC001, Youth Talent Promotion Project of Henan Province, 2023HYTP042

Availability of data and materials
All data needed to support the conclusions are present in the paper and/or the Supporting Information. Additional data related to this study are available from the corresponding authors upon reasonable.

Declarations

Ethics approval and consent to participate
The animal experiments were authorized by the Institutional Committee on the Ethics of Animal Experiments of Zhengzhou University (2023-KY-0433-001, Zhengzhou, China). All small animal experiments are carried out in accordance with the specifications of The National Regulation of China for Care and Use of Laboratory Animals, which have been approved by the Henan Administration of Experimental Animals.

Consent for publication
All the authors have approved the manuscript to publish.

Competing interests
The authors declare no competing interests.

Author details
[1]Department of Emergency Medicine, The First Affiliated Hospital of Zhengzhou University, Zhengzhou 450052, China. [2]Department of Orthopedics, The First Affiliated Hospital of Zhengzhou University, Zhengzhou 450052, China. [3]State Key Laboratory of Organic Electronics and Information Displays & Institute of Advanced Materials (IAM), Jiangsu Key Laboratory for Biosensors, Nanjing University of Posts & Telecommunications, Nanjing 210023, China. [4]Department of Gynecology, The First Affiliated Hospital of Zhengzhou University, Zhengzhou 450052, China.

Received: 2 June 2024 Accepted: 24 July 2024
Published online: 30 July 2024

References

1. Gottesman MM, Fojo T, Bates SE. Multidrug resistance in cancer: role of ATP–dependent transporters. Nat Rev Cancer. 2002;2(1):48–58.
2. Markman JL, Rekechenetskiy A, Holler E, Ljubimova JY. Nanomedicine therapeutic approaches to overcome cancer drug resistance. Adv Drug Deliv Rev. 2013;65(13):1866–79.
3. Jiang Z, Zhang C, Wang X, Yan M, Ling Z, Chen Y, Liu Z. A borondifluoride-complex-based photothermal agent with an 80 % photothermal conversion efficiency for photothermal therapy in the NIR-II window. Angew Chem Int Ed. 2021;60(41):22376–84.
4. Li S, Deng Q, Zhang Y, Li X, Wen G, Cui X, Wan Y, Huang Y, Chen J, Liu Z, Wang L, Lee C-S. Rational design of conjugated small molecules for superior photothermal theranostics in the NIR-II biowindow. Adv Mater. 2020;32(33):2001146.
5. Liu Y-Z, Ran X-Y, Zhou D-H, Zhang H, Chen Y-J, Xu J-X, Chen S-Y, Kong Q-Q, Yu X-Q, Li K. Novel dibenzofulvene-based NIR-II emission phototheranostic agent with an 82.6% photothermal conversion efficiency for photothermal therapy. Adv Funct Mater. 2024;34(8):2311365.
6. Li D, Zhang C, Tai X, Xu D, Xu J, Sun P, Fan Q, Cheng Z, Zhang Y. 1064 nm activatable semiconducting polymer-based nanoplatform for NIR-II fluorescence/NIR-II photoacoustic imaging guided photothermal therapy of orthotopic osteosarcoma. Chem Eng J. 2022;445:136836.
7. Gao Y, Liu Y, Li X, Wang H, Yang Y, Luo Y, Wan Y, Lee C-S, Li S, Zhang X-H. A stable open-shell conjugated diradical polymer with ultra-high photothermal conversion efficiency for NIR-II photo-immunotherapy of metastatic tumor. Nano-Micro Lett. 2023;16(1):21.
8. Long Z, Hu J-J, Yuan L, Duan C, Dai J, Zhen S, Zhao Z, Lou X, Xia F. A cell membrane-anchored nanoassembly with self-reporting property for enhanced second near-infrared photothermal therapy. Nano Today. 2021;41:101312.
9. Sun P, Qu F, Zhang C, Cheng P, Li X, Shen Q, Li D, Fan Q. NIR-II excitation phototheranostic platform for synergistic photothermal therapy/chemotherapy/chemodynamic therapy of breast cancer bone metastases. Adv Sci. 2022;9(33):2204718.
10. Wang Q, Dai Y, Xu J, Cai J, Niu X, Zhang L, Chen R, Shen Q, Huang W, Fan Q. All-in-one phototheranostics: single laser triggers NIR-II fluorescence/photoacoustic imaging guided photothermal/photodynamic/chemo combination therapy. Adv Func Mater. 2019;29(31):1901480.
11. Xiao P, Sun Y, Liang M, Yang S, Li J, Zhang LE, Jiang X, Wu W. A fluorophore with dithienopyrrole donor for beyond 1300 nm NIR-II fluorescence/photoacoustic dual-model imaging and photothermal therapy. Mater Today Nano. 2023;24:100404.
12. Chen Y, Chen S, Yu H, Wang Y, Cui M, Wang P, Sun P, Ji M. D-A type NIR-II organic molecules: strategies for the enhancement fluorescence brightness and applications in NIR-II fluorescence imaging-navigated photothermal therapy. Adv Healthcare Mater. 2022;11(21):2201158.
13. Ran X-Y, Chen P, Liu Y-Z, Shi L, Chen X, Liu Y-H, Zhang H, Zhang L-N, Li K, Yu X-Q. Rational design of polymethine dyes with NIR-II emission and high photothermal conversion efficiency for multimodal-imaging-guided photo-immunotherapy. Adv Mater. 2023;35(12):2210179.
14. Ma G, Liu Z, Zhu C, Chen H, Kwok RTK, Zhang P, Tang BZ, Cai L, Gong P. H2O2-responsive NIR-II AIE nanobomb for carbon monoxide

boosting low-temperature photothermal therapy. Angew Chem Int Ed. 2022;61(36): e202207213.
15. Fang Z, Zhang J, Shi Z, Wang L, Liu Y, Wang J, Jiang J, Yang D, Bai H, Peng B, Wang H, Huang X, Li J, Li L, Huang W. A gas/phototheranostic nanocomposite integrates NIR-II-peak absorbing Aza-BODIPY with thermal-sensitive nitric oxide donor for atraumatic osteosarcoma therapy. Adv Mater. 2023;35(35):2301901.
16. Wu G-L, Liu F, Li N, Fu Q, Wang C-K, Yang S, Xiao H, Tang L, Wang F, Zhou W, Wang W, Kang Q, Li Z, Lin N, Wu Y, Chen G, Tan X, Yang Q. Trisulfide bond-mediated molecular phototheranostic platform for "activatable" NIR-II imaging-guided enhanced gas/chemo-hypothermal photothermal therapy. Adv Sci. 2023;10(36):2304104.
17. Sun Z, Li T, Wu F, Yao T, Yang H, Yang X, Yin H, Gao Y, Zhang Y, Li C, Wang Q. Precise synergistic photothermal therapy guided by accurate temperature-dependent NIR-II fluorescence imaging. Adv Func Mater. 2024;34(14):2311622.
18. Xu Y, Teng C, Wang Y, Chen D, Yin D, Yan L. Self-enhanced regulation of stable organic radicals with polypeptide nanoparticles for mild second near-infrared phototheranostics. J Colloid Interface Sci. 2024;669:578–89.
19. Chen F, Liu L, Tang D, Zhang H, Wu N, Wang L, Li H, Xiao H, Zhou D. Treatment of acute wound infections by degradable polymer nanoparticle with a synergistic photothermal and chemodynamic strategy. Adv Sci. 2024;11(17):2309624.
20. Zhang X, Yang Y, Kang T, Wang J, Yang G, Yang Y, Lin X, Wang L, Li K, Liu J, Ni J-S. NIR-II absorbing semiconducting polymer-triggered gene-directed enzyme prodrug therapy for cancer treatment. Small. 2021;17(23):2100501.
21. Wei D, Sun Y, Zhu H, Fu Q. Stimuli-responsive polymer-based nanosystems for cancer theranostics. ACS Nano. 2023;17(23):23223–61.
22. Wei D, Fan J, Yan J, Liu C, Cao J, Xu C, Sun Y, Xiao H. Nuclear-targeting lipid PtIV prodrug amphiphile cooperates with siRNA for enhanced cancer immunochemotherapy by amplifying Pt-DNA adducts and reducing phosphatidylserine exposure. J Am Chem Soc. 2024;146(1):1185–95.
23. Sun K, Yuan L, Chen S, Sun Y, Wei D. Alendronate PtIV prodrug amphiphile for enhanced chemotherapy targeting and bone destruction inhibition in osteosarcoma. Adv Healthcare Mater. 2024;13(7):2302746.
24. Liu R, Peng Y, Lu L, Peng S, Chen T, Zhan M. Near-infrared light-triggered nano-prodrug for cancer gas therapy. J Nanobiotechnol. 2021;19(1):443.
25. Fu Y-J, Zhao X, Wang L-Y, Li K, Jiang N, Zhang S-T, Wang R-K, Zhao Y-F, Yang W. A gas therapy strategy for intestinal flora regulation and colitis treatment by nanogel-based multistage NO delivery microcapsules. Adv Mater. 2024;36(19):2309972.
26. Yu H, Tiemuer A, Yao X, Zuo M, Wang H-Y, Liu Y, Chen X. Mitochondria-specific near-infrared photoactivation of peroxynitrite upconversion luminescent nanogenerator for precision cancer gas therapy. Acta Pharmaceutica Sinica B. 2024;14(1):378–91.
27. Cheng P, Chen S, Li J, Yang W, Chen P, Miao H, Shen Q, Sun P, Fan Q. A noncovalent backbone planarization strategy increases the NIR-II extinction coefficients for gas/phototheranostic applications. Chem Commun. 2024;60(3):332–5.
28. Guo B, Chen J, Chen N, Middha E, Xu S, Pan Y, Wu M, Li K, Liu C, Liu B. High-resolution 3D NIR-II photoacoustic imaging of cerebral and tumor vasculatures using conjugated polymer nanoparticles as contrast agent. Adv Mater. 2019;31(25):1808355.
29. Men X, Wang F, Chen H, Liu Y, Men X, Yuan Y, Zhang Z, Gao D, Wu C, Yuan Z. Ultrasmall semiconducting polymer dots with rapid clearance for second near-infrared photoacoustic imaging and photothermal cancer therapy. Adv Func Mater. 2020;30(24):1909673.
30. Yin C, Tai X, Li X, Tan J, Lee C-S, Sun P, Fan Q, Huang W. Side chain engineering of semiconducting polymers for improved NIR-II fluorescence imaging and photothermal therapy. Chem Eng J. 2022;428:132098.
31. Sun P, Jiang X, Sun B, Wang H, Li J, Fan Q, Huang W. Electron-acceptor density adjustments for preparation conjugated polymers with NIR-II absorption and brighter NIR-II fluorescence and 1064 nm active photothermal/gas therapy. Biomaterials. 2022;280:121319.
32. Yin C, Zhang H, Sun B, Chen S, Jiang X, Miao X, Sun P, Hu W, Fan Q, Huang W. Remarkable suppression of vibrational relaxation in organic semiconducting polymers by introducing a weak electron donor for improved NIR-II phototheranostics. Adv Func Mater. 2021;31(47):2106575.
33. Sun P, Yang Z, Qu F, Du X, Shen Q, Fan Q. Conjugated/nonconjugated alternating copolymers for enhanced NIR-II fluorescence imaging and NIR-II photothermal-ferrotherapy. J Mater Chem B. 2022;10(47):9830–7.
34. Zhang R, Bi Z, Zhang L, Yang H, Wang H, Zhang W, Qiu Z, Zhang C, Xiong Y, Li Y, Zhao Z, Tang BZ. Blood circulation assessment by steadily fluorescent near-infrared-II aggregation-induced emission nano contrast agents. ACS Nano. 2023;17(19):19265–74.
35. Shen H, Sun F, Zhu X, Zhang J, Ou X, Zhang J, Xu C, Sung HHY, Williams ID, Chen S, Kwok RTK, Lam JWY, Sun J, Zhang F, Tang BZ. Rational design of NIR-II AIEgens with ultrahigh quantum yields for photo- and Chemiluminescence imaging. J Am Chem Soc. 2022;144(33):15391–402.
36. Liang M, Liu L, Sun Y, Li J, Zhang LE, Jiang X, Wu W. Furan-modified thiadiazolo quinoxaline as an electron acceptor for constructing second near-infrared aggregation-induced emission fluorophores for beyond 1300 nm fluorescence/photoacoustic imaging and photothermal therapy. Aggregate. 2024;5(2): e458.
37. Bian S, Zheng X, Liu W, Li J, Gao Z, Ren H, Zhang W, Lee C-S, Wang P. Pyrrolopyrrole aza-BODIPY-based NIR-II fluorophores for in vivo dynamic vascular dysfunction visualization of vascular-targeted photodynamic therapy. Biomaterials. 2023;298:122130.

Publisher's Note

Springer Nature remains neutral with regard to jurisdictional claims in published maps and institutional affiliations.